

Geophysical Research Letters®

RESEARCH LETTER

10.1029/2021GL096941

Key Points:

- We have solved the bounce-averaged quasi-linear diffusion equation along a Mars crustal field line to study wave-particle interactions
- Steady-state due to photoelectron resonance with whistler mode waves was reached on the order of minutes
- Both previous data-model discrepancies are resolved: a high energy perpendicular flux peak and increased isotropy

Correspondence to:

A. D. Shane,
adshane@umich.edu


Citation:

Shane, A. D., & Liemohn, M. W. (2022). Modeling wave-particle interactions with photoelectrons on the dayside crustal fields of Mars. *Geophysical Research Letters*, 49, e2021GL096941. <https://doi.org/10.1029/2021GL096941>

Received 5 NOV 2021

Accepted 4 JAN 2022

Modeling Wave-Particle Interactions With Photoelectrons on the Dayside Crustal Fields of Mars

Alexander D. Shane¹  and Michael W. Liemohn¹ 

¹Department of Climate and Space Sciences and Engineering, University of Michigan, Ann Arbor, MI, USA

Abstract Whistler mode waves have been proposed as a crucial mechanism in determining the velocity-space distribution of electrons on the dayside crustal magnetic fields of Mars. A superthermal electron transport model has been unable to reproduce the observed pitch angle distributions on a crustal field line. The two key differences are that the observed pitch angle distributions are much more isotropic and the observed high energy pitch angle distributions have a flux peak at perpendicular pitch angles. We solve the bounce-averaged quasi-linear diffusion equation to calculate the steady-state pitch angle distribution of electrons along a crustal field line when in resonance with whistler mode waves. We perform two simulations, changing the background ionosphere, which affects what energies are in resonance with the whistler mode wave. The wave parameters are chosen based on previous observations of whistlers at Mars. Our results reconcile both qualitative differences between the previous data-model comparisons.

Plain Language Summary An understanding of how electrons move through space environments is important for a multitude of reasons. It tells us where electrons will transfer their energy to the neutral atmosphere and it can indirectly inform us of where the magnetic field lines are connected to (the planet or solar wind). If the physical processes that control electron transport are unknown, then incorrect assumptions may be made. At Mars, our satellite observations and numerical simulations have not agreed, indicating that we do not include all the relevant physics in our models. Whistler mode waves are extremely low frequency radio waves that interact with electrons and can change the direction they are moving and increase their velocity. In this study, we simulate the effect of whistler mode waves on electrons at Mars. We find that our simulation results agree quite well with the data and reconciles the two key qualitative differences between previous data-model comparisons.

1. Introduction

The unique and dynamic magnetic field environment of Mars offers a fascinating laboratory to study space physics. Crustal magnetic fields cover the surface of the planet and rotate in and out of interaction with the solar wind. The strongest crustal fields are in the southern hemisphere and have a structure similar to coronal arcades on the surface of the Sun. In between these mini-magnetospheres are cusp regions allowing the solar wind access to the upper atmosphere of Mars. A myriad of plasma processes have been studied on the crustal fields including magnetic reconnection (e.g., Brain et al., 2010; Hara et al., 2017; Harada et al., 2018), solar wind precipitation (e.g., Mitchell et al., 2001; Xu et al., 2014), aurora (e.g., Bertaux et al., 2005; Brain et al., 2006; Dubinin et al., 2009; Schneider et al., 2018, 2021), and the influence of the crustal fields on atmospheric escape (e.g., Dubinin et al., 2020; Fang et al., 2015; Fan et al., 2019; Weber et al., 2021). Photoelectrons, produced by ionization of neutrals by solar radiation, populate these crustal fields on the dayside. These electrons have energies between 1 and 500 eV and are important for the energy budget of planetary atmospheres (see Coates et al., 2011 for a review). Furthermore, their distinct energy spectrum from solar wind electrons, is used to infer the magnetic topology (e.g., Xu et al., 2017, 2019).

Previous studies have revealed that our understanding of the transport of photoelectrons on dayside-closed crustal fields at Mars is incomplete. Shane et al. (2019) showed the modeled pitch angle distribution (PAD) of superthermal electrons on an ideal dipole crustal magnetic field generated from the superthermal electron transport (STET) model (e.g., Khazanov & Liemohn, 1995; Khazanov et al., 1993; Xu & Liemohn, 2015). This model predicts a source cone distribution for all energies and the higher the energy the more anisotropic the PAD is. This is due to the Coulomb collision frequency being proportional to $\propto \frac{1}{E^2}$. A case study (Liemohn et al., 2003) and statistical survey (Brain et al., 2007) of electron PADs using data from the Mars Global Surveyor (MGS)

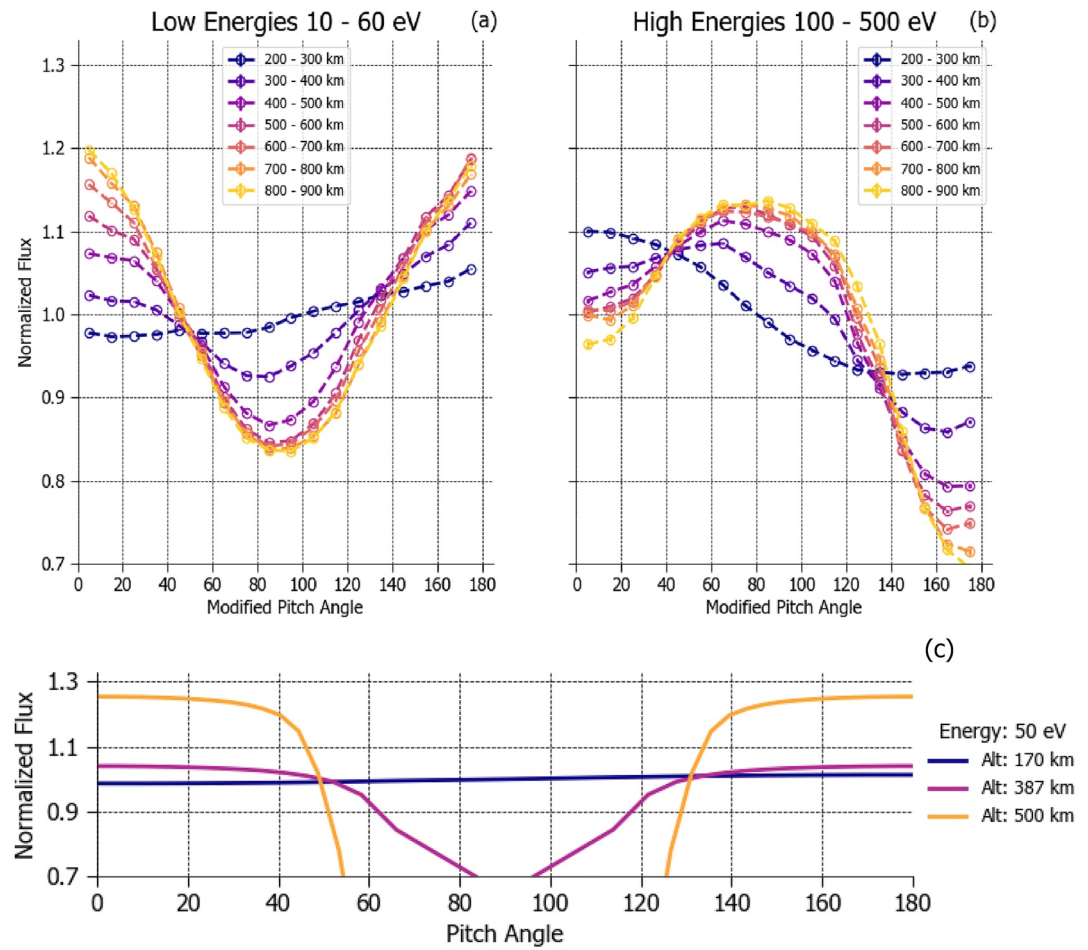


Figure 1. Figures from Shane et al. (2019) (a–b) MAVEN Data: Two year (December 2014–December 2016) averaged PADs for low and high energy electrons as a function of altitude. The data set is filtered for dayside-closed crustal fields and normalized to the average flux in each energy channel. (c) STET Output: 50 eV PADs as a function of altitude, with the same y-axis, highlighting the isotropy seen in the data.

electron reflectometer instrument (Mitchell et al., 2001) both measured isotropic or loss cone distributions for high energy electrons (>100 eV). Shane et al. (2019) used data from the solar wind electron analyzer (SWEA; Mitchell et al., 2016) onboard the Mars Atmosphere and Volatile Evolution (MAVEN; Jakosky et al., 2015) mission, filtered for dayside-closed crustal fields, and confirmed that on average, with no local time dependence observed, the high energy (100–500 eV) PADs had a loss cone distribution, contrary to the expected source cone distribution that is typical for photoelectrons. Furthermore, while the lower energy electrons (10–60 eV) did exhibit a source cone, it was much more isotropic (i.e., less anisotropic) than the STET modeling results. Some of these results from Shane et al. (2019) are displayed in Figure 1. Figures 1a and 1b are MAVEN observations. These show two year averaged normalized PADs as a function of altitude for low and high energies. The flux in each energy channel is normalized to the average flux in that energy channel. Figure 1c plots the altitude dependence of 50 eV PADs as calculated by STET. The y-axes are kept constant between the two data sets, highlighting the isotropy in the data. The high energy loss cone is seen at nearly all altitudes by MAVEN.

An external source of hot electrons could explain the flux peak at perpendicular pitch angles. However, the flux peak is observed on deep closed fields (strong magnetic field strength and quasi-horizontal magnetic elevation angle) and a local-time independent supply mechanism has not been proposed. Shane et al. (2019) hypothesized that resonant interactions with whistler mode waves are the missing physics in the STET model. Whistler mode waves are electromagnetic waves with frequencies between the local lower hybrid frequency and electron gyrofrequency. They are generated from temperature anisotropies in the electron velocity space distribution. These waves have been observed at Mars (Fowler et al., 2018, 2020; Harada et al., 2016) and their interaction with

superthermal electrons is energy-dependent (e.g., Liemohn et al., 1997; Lyons, 1974b). Through resonant interactions, whistler waves can energize and pitch angle scatter electrons, which could explain both the perpendicular flux peak at high energies and the increased isotropy at all energies.

Shane and Liemohn (2021) investigated the average plasma environment of the dayside-closed crustal fields to determine if the conditions are right for whistler mode waves to interact with electrons at the energies of interest. The characteristic energy, a function of the magnetic field strength and thermal electron density, is one quantity that determines the electron resonant energy. MAVEN measures both quantities, and Shane and Liemohn (2021) used typical altitude profiles of the characteristic energy to calculate bounce-averaged diffusion coefficients of the wave-particle interaction. The wave frequency and wave normal angle were set using the observations made by Harada et al. (2016) and Fowler et al. (2020). Their results showed that the wave-particle interaction process would be much faster than collisional processes. Timescales for low energy electron wave-particle interactions were fast and allowed for mixing with the source cone. At high energies the timescales were much slower, and restricted scattering across the source cone. Low energy electrons with perpendicular pitch angles energized to higher energies would then be trapped. These results help support the wave-particle interaction hypothesis proposed by Shane et al. (2019); however, modeling of the electron PADs is necessary to determine if this process is indeed a viable one.

In this paper, we will show our initial results of our modeling of the quasi-linear diffusion equation. This will be the first study of its kind at the planet Mars. The equation, in both its theoretical formulation and numerical implementation, will be discussed in Section 2. We will describe our model configuration (Section 3) and show results from two simulations (Section 4) using the same bounce-averaged diffusion coefficients as calculated in Shane and Liemohn (2021). In Section 5, we will discuss the results and future work.

2. Quasi-Linear Diffusion Equation

2.1. Theoretical Formulation

The quasi-linear diffusion equation was first derived by Kennel and Engelmann (1966) and later transformed into spherical coordinates by Lyons (1974a), shown here in Equation 1.

$$\frac{\partial f}{\partial t} = \frac{1}{v \sin(\alpha)} \frac{\partial}{\partial \alpha} \left\{ \frac{\sin(\alpha)}{v} D_{\alpha\alpha} \frac{\partial f}{\partial \alpha} + \sin(\alpha) D_{\alpha v} \frac{\partial f}{\partial v} \right\} + \frac{1}{v^2} \frac{\partial}{\partial v} \left\{ v D_{v\alpha} \frac{\partial f}{\partial \alpha} + v^2 D_{vv} \frac{\partial f}{\partial v} \right\} \quad (1)$$

Here, f is the electron distribution function, v is the velocity, α is the pitch angle, and D are the pitch angle, mixed, and velocity diffusion coefficients, which are functions of energy and pitch angle. To calculate the diffusion coefficients, a wave frequency and wave normal angle distribution must be assumed. Other inputs needed are the wave power and number of harmonics. Our choices for these inputs are discussed in Section 3. The expressions for the diffusion coefficients are quite expansive and will not be given here. We point the readers to Lyons (1974b), Jordanova et al. (1996), and Shane and Liemohn (2021) for detailed derivations. For this initial study, we omit the mixed diffusion terms as they are known to cause numerical issues. There are methods that can properly handle the mixed diffusion terms, such as the method used by Albert and Young (2005); however, this method was unsuccessful for our diffusion coefficient distribution. We note that the mixed terms become increasingly important for large characteristic energies and the characteristic energies used in this study are small. Nevertheless, a complete evaluation of the whistler wave effects on the electron distribution function would include the mixed diffusion terms. Furthermore, the diffusion coefficients we use are nonrelativistic as we are focused on electrons with energies less than 500 eV. A full relativistic formulation can be found in Glauert and Horne (2005) and Albert (2005).

We perform a change of variables using the following relations:

$$\begin{aligned} f &= \frac{m^2}{2E} \phi \\ v &= \sqrt{\frac{2E}{m}} \\ \frac{\partial \alpha_0}{\partial \alpha} &= \frac{B_0}{B} \frac{\sin(\alpha) \cos(\alpha)}{\sin(\alpha_0) \cos(\alpha_0)} = \frac{\tan(\alpha_0)}{\tan(\alpha)} \end{aligned} \quad (2)$$

where, m is the electron mass, ϕ is the electron differential number flux, E is the electron energy, and α_0 is the minimum-B pitch angle. The resulting equation is shown in Equation 3.

$$\frac{\partial \phi}{\partial t} = 2m\sqrt{E} \frac{\partial}{\partial E} \left\{ E^{\frac{3}{2}} D_{EE} \frac{\partial}{\partial E} \left\{ \frac{\phi}{E} \right\} \right\} + \frac{m}{2E \sin(\alpha)} \frac{\partial \alpha_0}{\partial \alpha} \frac{\partial}{\partial \alpha_0} \left\{ \sin(\alpha) D_{\alpha_0 \alpha_0} \frac{\partial \alpha_0}{\partial \alpha} \frac{\partial \phi}{\partial \alpha_0} \right\} \quad (3)$$

We now bounce-average Equation 3 resulting in our final equation:

$$\frac{\partial \phi}{\partial t} = 2m\sqrt{E} \frac{\partial}{\partial E} \left\{ E^{\frac{3}{2}} D_{EE}^{ba} \frac{\partial}{\partial E} \left\{ \frac{\phi}{E} \right\} \right\} + \frac{m}{2ES_0} \frac{1}{\sin(\alpha_0)\cos(\alpha_0)} \frac{\partial}{\partial \alpha_0} \left\{ S_0 \sin(\alpha_0)\cos(\alpha_0) D_{\alpha_0 \alpha_0}^{ba} \frac{\partial \phi}{\partial \alpha_0} \right\} \quad (4)$$

where, S_0 is the normalized quarter-bounce period and the bounce-averaged diffusion coefficients are calculated by:

$$\begin{aligned} S_0 &= \int_{s_1}^{s_2} \frac{ds}{\cos(\alpha)} \\ D_{EE}^{ba}(E, \alpha_0) &= \frac{1}{S_0} \int_{s_1}^{s_2} D_{EE}(E, \alpha) \frac{ds}{\cos(\alpha)} \\ D_{\alpha_0 \alpha_0}^{ba}(E, \alpha_0) &= \frac{1}{S_0} \int_{s_1}^{s_2} \left(\frac{\partial \alpha_0}{\partial \alpha} \right)^2 D_{\alpha\alpha}(E, \alpha) \frac{ds}{\cos(\alpha)} \end{aligned} \quad (5)$$

where, s_1 and s_2 are the base of the field line and top of the field line, respectively.

2.2. Numerical Implementation

The resulting bounce-averaged quasi-linear diffusion equation is a two-dimensional diffusion advection equation:

$$\frac{\partial \phi}{\partial t} = a \frac{\partial}{\partial E} \left\{ b \frac{\partial \phi}{\partial E} + c \phi \right\} + d \frac{\partial}{\partial \alpha_0} \left\{ e \frac{\partial \phi}{\partial \alpha_0} \right\} \quad (6)$$

where:

$$\begin{aligned} a &= \sqrt{E} \\ b &= 2m\sqrt{E} D_{EE}^{ba} \\ c &= -\frac{2m}{\sqrt{E}} D_{EE}^{ba} \\ d &= \frac{m}{2ES_0} \frac{1}{\sin(\alpha_0)\cos(\alpha_0)} \\ e &= S_0 \sin(\alpha_0)\cos(\alpha_0) D_{\alpha_0 \alpha_0}^{ba} \end{aligned} \quad (7)$$

We will use the Crank Nicolson (CN) and the Alternating Direction Implicit (ADI) methods to solve this equation. ADI allows us to split the calculation into two half time steps, with each variable alternating between implicit and explicit, giving two tridiagonal matrix inversions, speeding up the calculation with negligible cost to accuracy. Furthermore, this method is unconditionally stable in time providing a robust and fast solver of this equation. We use conservative forms of the finite difference approximations, requiring calculations of the coefficients at the grid boundaries and centers, and the fluxes are calculated at the grid centers. The whistler wave diffusion coefficients are therefore calculated on a 210×210 grid in energy-pitch angle space and the flux values will be calculated on a downsampled 105×105 grid. The velocity space domain where we solve the equation is from the source cone pitch angle ($\sim 24^\circ$ for this field line) to 90° and energies between 10 and 500 eV with $\Delta E = 4.09$ eV and $\Delta \alpha = 0.84^\circ$.

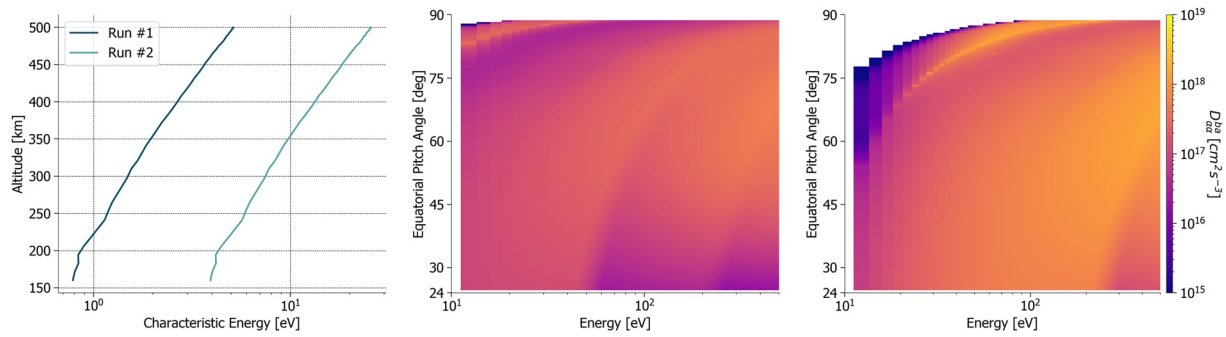


Figure 2. (Left) Characteristic energy altitude profiles for each run. This is the only difference between the two runs. (Middle) Bounce-averaged pitch angle diffusion coefficients for Run #1. (Right) Bounce-averaged pitch angle diffusion coefficients for Run #2.

3. Model Configuration

We will be solving this equation for the bounce-averaged differential number flux along a Mars crustal field line. The magnetic field configuration, atmosphere conditions, and whistler wave parameters will be identical to the bounce-averaged calculations of Shane and Liemohn (2021), specifically Runs #1 and #2. The magnetic field is an ideal dipole with a field strength of ~ 294 nT at the exobase (160 km) and 50 nT at the top of the field line (500 km). The background atmosphere and ionosphere is taken from MGITM (Bougher et al., 2015). Above 250 km, the log of the densities are linearly extrapolated. The wave parameters used are representative of the observations by Harada et al. (2016) and Fowler et al. (2020). The wave power is assumed to be 10^{-4} nT²/Hz. The wave normal angle distribution ranges from 0° to 45° and the wave frequency distribution ranges from $0.1\Omega_e^{eq}$ to $0.5\Omega_e^{eq}$, where Ω_e^{eq} is the local electron gyrofrequency at the top of the field line. Both distributions are assumed to be Gaussian with peaks at 0° and $0.25\Omega_e^{eq}$. We include harmonics $|m| \leq 5$.

Figure 2 (left) plots the characteristic energy profiles of each simulation. The characteristic energy is a multiplicative factor when calculating the parallel resonant energy of electrons (see Equations 2 and 3 in Shane & Liemohn, 2021). The local resonant energy of the electron can be either greater than or less than the local characteristic energy, depending on the particle's pitch angle. The characteristic energy is a function of the magnetic field strength and thermal electron density and therefore it is altitude dependent. A different thermal electron density profile is the only difference between the two runs. The characteristic energy profile in Run #1 matches the median altitude distribution measured by MAVEN on dayside crustal fields, and the profile in Run #2 matches the arithmetic mean altitude distribution observed. The resultant diffusion coefficient distributions are also plotted in Figure 2 (middle and right). Note that there are small regions of velocity space (low energies, perpendicular pitch angles) where resonance does not occur. This will be discussed below, however, this is the reason Run #3 of Shane and Liemohn (2021) was omitted from this study, as this region is much larger, and the interpretation of the PADs is quite difficult.

The initial conditions are taken from a steady-state run using the same magnetic field and atmosphere in the STET model. Figure 4 of Xu and Liemohn (2015) shows that the flux as a function of minimum-B pitch angle and distance along the magnetic field does not vary above the exobase and this analysis held true for our steady-state runs. The flux at the top of the field line is used as our initial conditions. At the energy grid boundaries and source cone boundary we use Dirichlet boundary conditions (flux = constant) and at $\alpha_0 = 90^\circ$ we implement a zero slope Neumann boundary condition. Figure 3 shows the initial conditions used in our modeling runs. Figure 3 plots the unnormalized and normalized velocity space distribution (left and right). The normalized full velocity space distribution has a saturated color scale in order to highlight the anisotropy that STET predicts. The scale is the same as that used in Shane et al. (2019) and in this study's output. The middle subfigure plots the normalized PADs for selected energies. The PAD for each energy is normalized to the average flux at that energy so different normalization factors are used between PADs. We remind the reader that the only source and loss terms incorporated into the STET model are collisions.

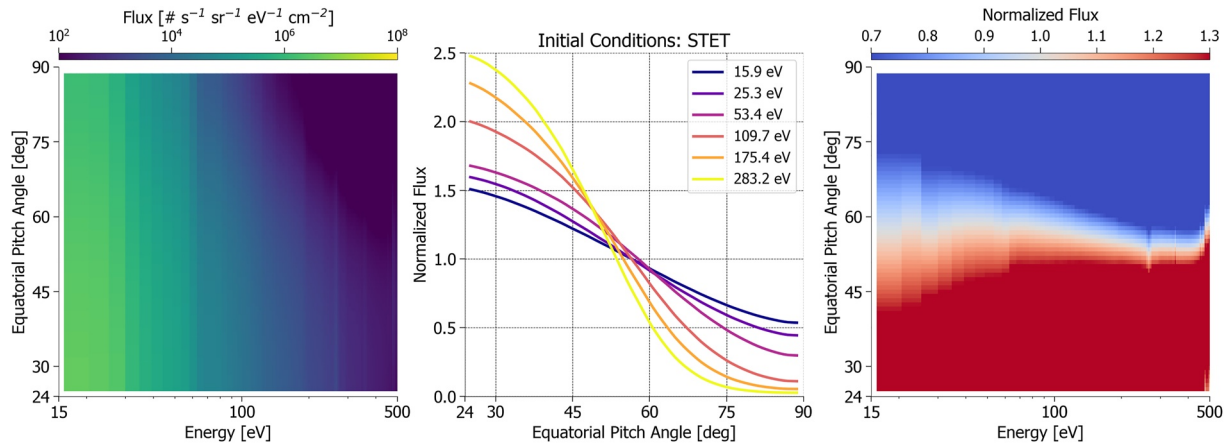


Figure 3. STET steady state results which are used as the initial condition for solving the bounce-averaged quasi-linear diffusion equation. (Left) Full initial velocity space distribution. (Middle) Normalized initial PADs for selected energies. (Right) Normalized initial full velocity space distribution.

4. Modeling Results

Figure 4 shows the steady-state fluxes for Runs #1 and #2, (top and bottom rows, respectively). Both of these rows are formatted the same as Figure 3 for direct comparison. Note that the y-axes of the middle plots have changed to match those of Shane et al. (2019). The time step used was 0.01 s and the final time was 200 s. We note that the lower energy electrons (<200 eV) reached steady state much earlier (<100 s). The diffusion coefficient resonance boundary can be most readily seen in the steady-state fluxes for Run #2. Additional physics terms are necessary to smooth this discontinuity out in the steady state results, with Coulomb collisions, the primary physical process controlling the electron distribution in the absence of waves, being the obvious candidate. Coulomb collisions primarily diffuse in pitch angle (but also de-energize) and so we could expect the distribution to be flat in the region

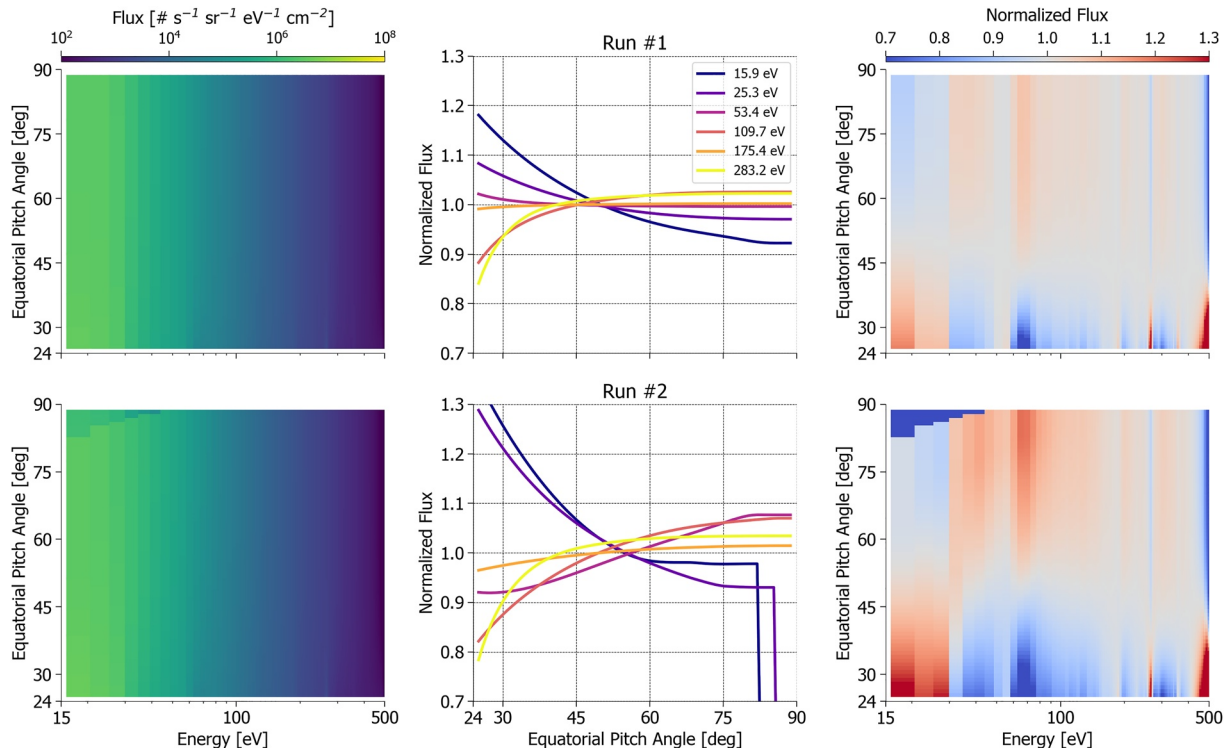


Figure 4. Steady-state fluxes at $t = 200$ s for Run #1 (top row) and Run #2 (bottom row). (Left) Full steady-state velocity space distribution. (Middle) Normalized steady-state PADs for selected energies. (Right) Normalized steady-state velocity space distribution.

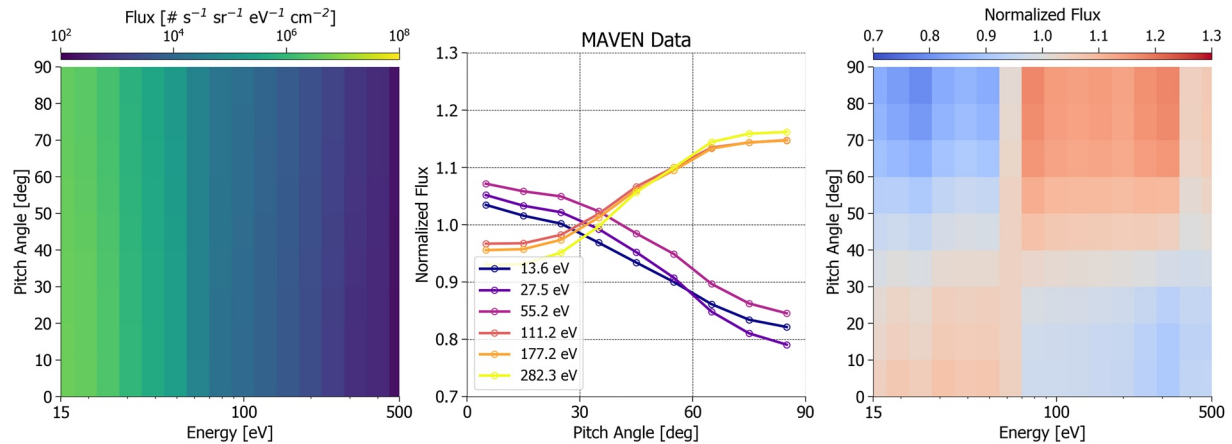


Figure 5. Two year averaged PADs measured by MAVEN on dayside crustal fields averaged around 90° pitch angle. Only measurements above 300 km are used. (Left) Full velocity space distribution. (Middle) Normalized PADs for selected energies. (Right) Normalized velocity space distribution.

of the discontinuity, however, this would occur on slower timescales. Alternatively, the frequency distribution of the whistler waves could be expanded such that these parallel energies are also in resonance. We have not done so here for continuity between the two runs and papers.

The major effect of whistler waves on the velocity space distribution of electrons has been to scatter particles into the trapped zone and isotropize. Any variation in flux with respect to pitch angle is barely noticeable by eye in the full unnormalized velocity space distribution. After normalizing to the average flux in each energy channel, the anisotropy becomes observable and on the same scale as the observations. The lowest energy electrons have a moderate source cone distribution, and most energies have a loss cone shape. The transition from source cone to loss cone is at a lower energy (~30 eV) than seen in the data (~60 eV). The loss cone shape is not due to a loss of electrons to the atmosphere, but is formed by energization of trapped electrons to these higher energies. Furthermore, sharp gradients in the photoelectron energy spectrum such as the photoelectron knee at ~60 eV and the Auger peaks at ~260 and ~500 eV can be easily seen in the steady-state results. These sharp transitions and large degree of anisotropy are not physical and are a product of the source cone boundary condition.

5. Discussion

Figure 5 plots the same data set as analyzed in Shane et al. (2019) but in the same format as our model output for direct comparison. Here, we have averaged around 90° pitch angle and only measurements above 300 km are used. The difference between STET and MAVEN observations is striking and there are two primary discrepancies between the STET model and MAVEN observations: the observed high energy PADs have a peak at perpendicular pitch angles and the observed PADs are more isotropic than the modeled PADs. Solving the quasi-linear diffusion equation with average measured characteristic energy profiles and using wave parameters observed at Mars have produced PADs that resolve these two differences. These simulations reveal that whistler waves are able to isotropize the velocity space distribution, and then energize the trapped low energy electrons to produce both the quasi-isotropic low energy source cone and high energy perpendicular peak as seen in the data. These are purely qualitative statements as we are comparing 2 year averaged observed PADs with steady state distributions using typical crustal field plasma environments and a single set of wave parameters. For example, the energies at which the PAD shifts from a source cone to loss cone is inconsistent between observations and model results. This is to be expected and is the result of averaging over many different wave distributions and characteristic energy profiles in the data. The steady-state fluxes obtained by solving the quasi-linear diffusion equation further support the wave-particle interaction hypothesis of what mechanism controls the electron distribution function on the dayside crustal magnetic fields of Mars.

While these model results greatly support our hypothesis, there are still questions to be answered. First is the recurrence rate of whistler mode waves necessary for this distribution to be prevalent on dayside crustal fields. One way to test this would be to include bounce-averaged collision terms in our model. After wave-particle

interaction steady-state is reached the waves could be switched off, and the time the distribution takes to relax to collision-only steady-state could be quantified. We are currently working on this as the relaxation time would be important in understanding the dynamics of the Mars crustal fields and would help put future measurements into context.

Second is the question of where the waves are generated and how they get onto the crustal fields. Harada et al. (2016) observed narrowband whistler mode wave events clustered near the nominal magnetic pileup boundary on the dayside. These waves may be produced in the magnetosheath and propagate onto the crustal fields. Ray tracing models should be employed to understand the trajectories of whistler waves in the Mars magnetosphere, perhaps gaining entry akin to chorus waves becoming plasmaspheric hiss in the Earth's inner magnetosphere (e.g., Bortnik et al., 2011). An understanding of the wave's reflection or absorption point at low altitudes is also necessary. The timescales to steady-state in this study were on the order of minutes. If the waves experience multiple reflections, then a single burst of waves may be sufficient to produce the observed distributions. If absorption occurs, multiple or sustained injections of waves would be necessary. A relaxation time estimate is also important here to quantify how often waves would need to be injected from the magnetosheath onto the magnetic crustal fields.

The assumption of quasi-linear theory should also be discussed. The validity of quasi-linear theory breaks down as the wave amplitude becomes large. Tao et al. (2012) compared test-particle simulation diffusion coefficients to those calculated from quasi-linear theory to quantify at what wave amplitude do the two sets of diffusion coefficients diverge. They found that the diffusion coefficients begin to differ by a factor of two when the normalized wave energy density, that is, the wave energy density divided by the background magnetic field energy density, is greater than 10^{-5} – 10^{-6} , depending on the energy and pitch angle. The normalized wave energy density in this study was 3.1×10^{-7} , justifying our use of quasi-linear theory. We note, however, that the energies of interest in this study are far lower than those investigated by Tao et al. (2012), so this exact threshold may not be applicable. Nonlinear effects tend to decrease the diffusion coefficients (Tao et al., 2012), therefore our calculated timescales to reach steady state may be taken as a lower limit.

6. Conclusions

In this study, we have solved the bounce-averaged quasi-linear diffusion equation in order to understand the effects of whistler mode waves on the electron PADs on dayside crustal magnetic fields. Our initial results have reconciled both qualitative differences between MAVEN observations and the STET model. The steady-state modeled low energy electron PADs are more isotropic and the high energy electron PADs have a flux peak at perpendicular pitch angles. While the energy at which the PADs switch from source cone to loss cone is inconsistent with the observations, this may be remedied by a wave parameter study. Whistler waves are a strong candidate as the dominant physical process controlling the electron distribution function on dayside crustal fields. The addition of mixed diffusion and collision terms to our model will greatly enhance the science return and efforts are currently underway to include them. More wave data at Mars is necessary to confirm our hypothesis and the impact on electron precipitation should be evaluated.

Data Availability Statement

All MAVEN data can be accessed through the Planetary Data System (<https://pds/ppi.igpp.ucla.edu/mission/MAVEN>). The Mars dayside crustal field PAD data set can be found at Shane (2121a). The input and output to the simulations can be found at Shane (2121b).

References

- Albert, J. M. (2005). Evaluation of quasi-linear diffusion coefficients for whistler mode waves in a plasma with arbitrary density ratio. *Journal of Geophysical Research: Space Physics*, 110(A3). <https://doi.org/10.1029/2004JA010844>
- Albert, J. M., & Young, S. L. (2005). Multidimensional quasi-linear diffusion of radiation belt electrons. *Geophysical Research Letters*, 32(14). <https://doi.org/10.1029/2005GL023191>
- Bertaux, J. L., Leblanc, F., Witasse, O., Quemerais, E., Lilensten, J., Stern, S. A., & Korabely, O. (2005). Discovery of an aurora on Mars. *Nature*, 435, 790–794. <https://doi.org/10.1038/nature03603>
- Bortnik, J., Chen, L., Li, W., Thorne, R. M., & Horne, R. B. (2011). Modeling the evolution of chorus waves into plasmaspheric hiss. *Journal of Geophysical Research*, 116(A8). <https://doi.org/10.1029/2011JA016499>

Acknowledgments

This work was supported by the National Aeronautics and Space Administration (NASA) grant NNX16AQ04G to the University of Michigan and the Rackham Predoctoral Fellowship. The authors thank Dr. Robert Krasny for discussions concerning numerical schemes and stability.

- Bougher, S. W., Pawlowski, D., Bell, J. M., Nelli, S., McDunn, T., Murphy, J. R., & Ridley, A. (2015). Mars global ionosphere-thermosphere model: Solar cycle, seasonal, and diurnal variations of the Mars upper atmosphere. *Journal of Geophysical Research: Planets*, *120*(2), 311–342. <https://doi.org/10.1002/2014JE004715>
- Brain, D. A., Baker, A. H., Briggs, J., Eastwood, J. P., Halekas, J. S., & Phan, T. D. (2010). Episodic detachment of Martian crustal magnetic fields leading to bulk atmospheric plasma escape. *Geophysical Research Letters*, *37*. <https://doi.org/10.1029/2010GL043916>
- Brain, D. A., Halekas, J. S., Peticolas, L. M., Lin, R. P., Luhmann, J. G., Mitchell, D. L., & Rème, H. (2006). On the origin of aurorae on Mars. *Geophysical Research Letters*, *33*, 1201. <https://doi.org/10.1029/2005GL024782>
- Brain, D. A., Lillis, R. J., Mitchell, D. L., Halekas, J. S., & Lin, R. P. (2007). Electron pitch angle distributions as indicators of magnetic field topology near Mars. *Journal of Geophysical Research*, *112*(A9), A09201. <https://doi.org/10.1029/2007JA012435>
- Coates, A. J., Tsang, S. M., Wellbrock, A., Frahm, R. A., Winningham, J. D., Barabash, S., & Crary, F. J. (2011). Ionospheric photoelectrons: Comparing Venus, Earth, Mars and Titan. *Planetary and Space Science*, *59*, 1019–1027. <https://doi.org/10.1016/j.pss.2010.07.016>
- Dubinin, E., Fraenz, M., Pätzold, M., Woch, J., McFadden, J., Fan, K., & Zelenyi, L. (2020). Impact of Martian crustal magnetic field on the ion escape. *Journal of Geophysical Research: Space Physics*, *125*, e2020JA028010. <https://doi.org/10.1029/2020JA028010>
- Dubinin, E., Fraenz, M., Woch, J., Barabash, S., & Lundin, R. (2009). Long-lived auroral structures and atmospheric losses through auroral flux tubes on Mars. *Geophysical Research Letters*, *36*. <https://doi.org/10.1029/2009GL038209>
- Fan, K., Fraenz, M., Wei, Y., Han, Q., Dubinin, E., Cui, J., & Connerney, J. E. (2019). Reduced atmospheric ion escape above Martian crustal magnetic fields. *Geophysical Research Letters*, *46*, 11764–11772. <https://doi.org/10.1029/2019GL084729>
- Fang, X., Ma, Y., Brain, D., Dong, Y., & Lillis, R. (2015). Control of Mars global atmospheric loss by the continuous rotation of the crustal magnetic field: A time-dependent MHD study. *Journal of Geophysical Research: Space Physics*, *120*(10), 926944–927010. <https://doi.org/10.1002/2015JA021605>
- Fowler, C. M., Agapitov, O. V., Xu, S., Mitchell, D. L., Andersson, L., Artemyev, A., & Mazelle, C. (2020). Localized heating of the Martian topside ionosphere through the combined effects of magnetic pumping by large-scale magnetosonic waves and pitch angle diffusion by whistler waves. *Geophysical Research Letters*, *47*(5). <https://doi.org/10.1029/2019GL086408>
- Fowler, C. M., Andersson, L., Ergun, R. E., Harada, Y., Hara, T., Collinson, G., & Jakosky, B. M. (2018). MAVEN observations of solar wind-driven magnetosonic waves heating the Martian dayside ionosphere. *Journal of Geophysical Research: Space Physics*, *123*(5), 4129–4149. <https://doi.org/10.1029/2018JA025208>
- Glauert, S. A., & Horne, R. B. (2005). Calculation of pitch angle and energy diffusion coefficients with the PADIE code. *Journal of Geophysical Research*, *110*(A4). <https://doi.org/10.1029/2004JA010851>
- Hara, T., Brain, D. A., Mitchell, D. L., Luhmann, J. G., Seki, K., Hasegawa, H., & Jakosky, B. M. (2017). MAVEN observations of a giant ionospheric flux rope near Mars resulting from interaction between the crustal and interplanetary draped magnetic fields. *Journal of Geophysical Research: Space Physics*, *122*, 828–842. <https://doi.org/10.1002/2016JA023347>
- Harada, Y., Andersson, L., Fowler, C. M., Mitchell, D. L., Halekas, J. S., Mazelle, C., & Jakosky, B. M. (2016). MAVEN observations of electron-induced whistler mode waves in the Martian magnetosphere. *Journal of Geophysical Research: Space Physics*, *121*(10), 9717–9731. <https://doi.org/10.1002/2016JA023194>
- Harada, Y., Halekas, J. S., DiBraccio, G. A., Xu, S., Espley, J., McFadden, J. P., & Jakosky, B. M. (2018). Magnetic reconnection on dayside crustal magnetic fields at Mars: MAVEN observations. *Geophysical Research Letters*, *45*, 4550–4558. <https://doi.org/10.1002/2018GL077281>
- Jakosky, B. M., Lin, R. P., Grebowsky, J. M., Luhmann, J. G., Mitchell, D. F., Beutelschies, G., & Zurek, R. (2015). The Mars atmosphere and volatile evolution (Maven) mission. *Space Science Reviews*, *195*(1), 3–48. <https://doi.org/10.1007/s11214-015-0139-x>
- Jordanova, V. K., Kozyra, J. U., & Nagy, A. F. (1996). Effects of heavy ions on the quasi-linear diffusion coefficients from resonant interactions with electromagnetic ion cyclotron waves. *Journal of Geophysical Research*, *101*(A9), 19771–19778. <https://doi.org/10.1029/96JA01641>
- Kennel, C. F., & Engelmann, F. (1966). Velocity space diffusion from weak plasma turbulence in a magnetic field. *The Physics of Fluids*, *9*(12), 2377–2388. <https://doi.org/10.1063/1.1761629>
- Khazanov, G. V., & Liemohn, M. W. (1995). Nonsteady state ionosphere-plasmasphere coupling of superthermal electrons. *Journal of Geophysical Research*, *100*(A6), 9669–9681. <https://doi.org/10.1029/95JA00526>
- Khazanov, G. V., Liemohn, M. W., Gombosi, T. I., & Nagy, A. F. (1993). Non-steady-state transport of superthermal electrons in the plasmasphere. *Geophysical Research Letters*, *20*(24), 2821–2824. <https://doi.org/10.1029/93GL03121>
- Liemohn, M. W., Khazanov, G. V., & Kozyra, J. U. (1997). Guided plasmaspheric hiss interactions with superthermal electrons 1. Resonance curves and timescales. *Journal of Geophysical Research*, *102*(6), 11619–11623. <https://doi.org/10.1029/97JA00825>
- Liemohn, M. W., Mitchell, D. L., Nagy, A. F., Fox, J. L., Reimer, T. W., & Ma, Y. (2003). Comparisons of electron fluxes measured in the crustal fields at Mars by the MGS magnetometer/electron reflectometer instrument with a B field-dependent transport code. *Journal of Geophysical Research: Planets*, *108*(E12). <https://doi.org/10.1029/2003JE002158>
- Lyons, L. R. (1974a). General relations for resonant particle diffusion in pitch angle and energy. *Journal of Plasma Physics*, *12*(1), 45–49. <https://doi.org/10.1017/S0022377800024910>
- Lyons, L. R. (1974b). Pitch angle and energy diffusion coefficients from resonant interactions with ion-cyclotron and whistler waves. *Journal of Plasma Physics*, *12*(3), 417–432. <https://doi.org/10.1017/S002237780002537X>
- Mitchell, D. L., Lin, R. P., Mazelle, C., Rème, H., Cloutier, P. A., Connerney, J. E. P., & Ness, N. F. (2001). Probing Mars' crustal magnetic field and ionosphere with the mgs electron reflectometer. *Journal of Geophysical Research*, *106*(E10), 23419–23427. <https://doi.org/10.1029/2000JE001435>
- Mitchell, D. L., Mazelle, C., Sauvaud, J.-A., Thocaven, J.-J., Rouzaud, J., Fedorov, A., & Jakosky, B. M. (2016). The MAVEN solar wind electron analyzer. *Space Science Reviews*, *200*(1), 495–528. <https://doi.org/10.1007/s11214-015-0232-1>
- Schneider, N. M., Jain, S. K., Deighan, J., Nasr, C. R., Brain, D. A., Larson, D., & Jakosky, B. M. (2018). Global aurora on Mars during the September 2017 space weather event. *Geophysical Research Letters*, *45*, 7391–7398. <https://doi.org/10.1029/2018GL077772>
- Schneider, N. M., Milby, Z., Jain, S. K., Gérard, J.-C., Soret, L., Brain, D. A., & Jakosky, B. M. (2021). Discrete aurora on Mars: Insights into their distribution and activity from MAVEN/UVS observations. *Journal of Geophysical Research: Space Physics*, *126*, e2021JA029428. <https://doi.org/10.1029/2021JA029428>
- Shane, A. (2021a). *Mars Dayside Closed Crustal Field Electron Pitch Angle Distributions Data and Ephemeris Info* [Data set]. University of Michigan - Deep Blue Data. <https://doi.org/10.7302/ya0j-kh60>
- Shane, A. (2021b). *Bounce-Averaged Quasi-Linear Diffusion Model Simulation Input/Output on Mars' Crustal Magnetic Field* [Data set]. University of Michigan - Deep Blue Data. <https://doi.org/10.7302/43d3-1867>
- Shane, A., & Liemohn, M. (2021). Whistler wave interactions with superthermal electrons on Martian crustal magnetic fields: Bounce-averaged diffusion coefficients and time scales. *Journal of Geophysical Research: Space Physics*, *126*(6). <https://doi.org/10.1029/2021JA029118>

- Shane, A., Liemohn, M., Florie, C., & Xu, S. (2019). Misbehaving high-energy electrons: Evidence in support of ubiquitous wave-particle interactions on dayside Martian closed crustal magnetic fields. *Geophysical Research Letters*, *46*(21), 11689–11697. <https://doi.org/10.1029/2019GL084919>
- Tao, X., Bortnik, J., Albert, J. M., & Thorne, R. M. (2012). Comparison of bounce-averaged quasi-linear diffusion coefficients for parallel propagating whistler mode waves with test particle simulations. *Journal of Geophysical Research: Space Physics*, *117*(A10). <https://doi.org/10.1029/2012JA017931>
- Weber, T., Brain, D., Xu, S., Mitchell, D., Espley, J., Mazelle, C., & Jakosky, B. (2021). Martian crustal field influence on o+ and o2+ escape as measured by MAVEN. *Journal of Geophysical Research: Space Physics*, *126*, e2021JA029234. <https://doi.org/10.1029/2021JA029234>
- Xu, S., & Liemohn, M. W. (2015). Superthermal electron transport model for Mars. *Earth and Space Science*, *2*(3), 47–64. <https://doi.org/10.1002/2014EA000043>
- Xu, S., Liemohn, M. W., & Mitchell, D. L. (2014). Solar wind electron precipitation into the dayside Martian upper atmosphere through the cusps of strong crustal fields. *Journal of Geophysical Research: Space Physics*, *119*, 10100–10115. <https://doi.org/10.1002/2014JA020363>
- Xu, S., Mitchell, D., Liemohn, M., Fang, X., Ma, Y., Luhmann, J., & Jakosky, B. (2017). Martian low-altitude magnetic topology deduced from MAVEN/SWEA observations. *Journal of Geophysical Research: Space Physics*, *122*(2), 1831–1852. <https://doi.org/10.1002/2016JA023467>
- Xu, S., Weber, T., Mitchell, D. L., Brain, D. A., Mazelle, C., DiBraccio, G. A., & Espley, J. (2019). A technique to infer magnetic topology at Mars and its application to the terminator region. *Journal of Geophysical Research: Space Physics*, *124*, 1823–1842. <https://doi.org/10.1029/2018JA026366>